Arch. Metall. Mater. **67** (2022), 3, 1185-1193

DOI: https://doi.org/10.24425/amm.2022.139719

M. WÓJCIK[1*], A. SKRZAT[1]

COUPLED THERMOMECHANICAL EULERIAN-LAGRANGIAN ANALYSIS OF THE KOBO EXTRUSION PROCESS

Numerical simulations of the KOBO extrusion process are presented in this paper. The coupled thermomechanical Eulerian-Lagrangian approach was applied for the three-dimensional finite element model. The dynamic explicit Euler forward method was used in numerical calculations. The elastic-plastic Chaboche model assuming isotropic and kinematic hardening under variable temperature conditions was applied to describe the behaviour of the material under cyclic loading. In numerical computations Chaboche material model implemented in commercial software, as well as the proprietary one written as FORTRAN procedure were tested. The numerical results present the stress and strain distributions in the extruded material, as well as an increase of temperature due to the plastic work and friction. The shape of plastic strain zones was verified experimentally. The approach presented in the paper is a promising numerical tool to simulate the KOBO process.

Keywords: KOBO extrusion; Chaboche model; coupled Eulerian-Lagrangian analysis; SPD method; plasticity

1. Introduction

The extrusion is one of the most commonly used conventional forming processes that determines the possibility to obtain complex products with beneficial structure and properties. Compared to other metal-forming processes, the extrusion enables to obtain high elongation up to several hundred percent. Therefore, the method has attracted increasing attention in an industry, including the automotive and aviation sectors. However, the conventional extrusion takes disadvantages associated with the high forces necessary to deform the material and with the accelerated tools wear. The KOBO process was introduced to minimize or even eliminate disadvantages of the conventional extrusion.

The KOBO method is an unconventional elastic-plastic deformation process classified to cyclic severe plastic deformation (SPD) methods assisted by a cyclic rotation of the die with a given frequency and by a certain angle that results in the change of a material structure [1]. The reduction of a strain work and a decrease of the temperature of the process are the main technological advantages of the KOBO extrusion. It determines the cold forming of heavily deformed materials and the production of goods with a complex geometry with a decrease of the tools wear, simultaneously. Theoretical basics of the process are described in [2-5].

Numerical simulations of the extrusion process were carried out previously, and there are a lot of papers concerning this subject in the literature. In [6], the results of numerical calculations of the aluminum profile extrusion are presented. The changes of the isothermal temperature, as well as the stress and strain distribution are shown. The mesh distortion, the field of material flow and distributions of the stress and strain for sheet metal extrusion are analyzed in [7]. The experimental and numerical results of the extrusion of metallic composite materials using the updated Lagrangian and the coupled Eulerian-Lagrangian (CEL) approaches are described in [8]. The CEL method was also applied in the modelling of the backward extrusion in [9].

Only some efforts are available to model the KOBO extrusion process. At present, most of them are focused on the modelling of the change of microstructure in the wake of the rotation of the die. The evolution of crystallographic texture in the KOBO extrusion process was modelled in [10]. The modelling of microstructural changes in metals in the wake of a large plastic deformation in the KOBO process is shown in [11]. The numerical analysis of the axisymmetric extrusion assisted by cyclic torsion was presented in [12]. In authors' previous research

[1] RZESZOW UNIVERSITY OF TECHNOLOGY, FACULTY OF MECHANICAL ENGINEERING AND AERONAUTICS, DEPARTMENT OF MATERIALS FORMING AND PROCESSING, 8 POWSTAŃCÓW WARSZAWY AVE., 35-959 RZESZÓW, POLAND

* Corresponding author: m.wojcik@prz.edu.pl

© 2022. The Author(s). This is an open-access article distributed under the terms of the Creative Commons Attribution-NonCommercial License (CC BY-NC 4.0, https://creativecommons.org/licenses/by-nc/4.0/deed.en which permits the use, redistribution of the material in any medium or format, transforming and building upon the material, provided that the article is properly cited, the use is noncommercial, and no modifications or adaptations are made.

[13], numerical calculations of the KOBO extrusion using the coupled Eulerian-Lagrangian (CEL) analysis without taking into account the temperature were done.

In this paper the thermomechanical coupled Eulerian-Lagrangian approach was used to simulate the KOBO extrusion process.The elastic-plastic Chaboche material model, including both kinematic and isotropic strain hardening, was applied here. The proprietary material model written in a FORTRAN procedure was used in the commercial ABAQUS program. The correctness of the procedure applied was verified on the selected elastic-plastic problems. The distribution of stress, strain and temperature in the extruded material was analyzed. The change of the material behaviour during cyclic loading associated with the hardening was also examined. The results were also verified with experiments. The numerical simulations of the KOBO extrusion can contribute to the optimization of the process associated with the proper selection of the die rotation angle and frequency, and can lead to the minimization of the damage of tools (Fig. 1). Additionally, the application of the proprietary material model in numerical calculations enables to obtain better knowledge about the phenomena in the material during the KOBO extrusion process.

Fig. 1. Damage of dies and handles during the KOBO extrusion

2. Theory section

2.1. Continuum mechanics and the large strain theory

In SPD processes, including the KOBO extrusion, the extruded material is subjected to large plastic deformation. The large strain theory used in the user material procedures is presented here. In continuum mechanics, two material configurations – the reference, undeformed ($\mathcal{B}_0$) and current, deformed ($\mathcal{B}$) configurations are compared to describe the kinematics of a deformation of a material body [14]. If $x_0 \in \mathcal{B}_0$ is the initial position of a particle in the reference configuration at time $t = t_0$ and $x \in \mathcal{B}$ is the current position in the deformed configuration, the motion and the deformation of a continuum body will be described by a smooth time-dependent mapping function $\breve{\boldsymbol{x}}_t$ (Eq. 1):

$$\breve{\boldsymbol{x}}_t : \mathcal{B}_0 \rightarrow \mathcal{B} \; ; \; x = \breve{\boldsymbol{x}}(\boldsymbol{x}_0, t) \tag{1}$$

where: x is the position of a material particle at current time t.

The deformation of a continuum body in a large strain theory is characterized by the deformation gradient tensor ($\boldsymbol{F}$) (Eq. 2) which transforms the infinitesimal material vector $d\boldsymbol{x}_0 \in \mathcal{B}_0$ in the reference configuration into the corresponding spatial vector $d\boldsymbol{x} \in \mathcal{B}$ in the current configuration (Eq. 3).

$$\boldsymbol{F} = \frac{\partial \boldsymbol{x}}{\partial \boldsymbol{x}_0} = \nabla_0 \boldsymbol{x} \tag{2}$$

$$d\boldsymbol{x} = \boldsymbol{F}\, d\boldsymbol{x}_0 \tag{3}$$

where: ∇_0 is the left, material gradient operator and $\nabla_0 = \frac{\partial}{\partial \boldsymbol{x}_0}$.

The displacement ($\boldsymbol{u}$) and velocity ($\boldsymbol{v}$) vectors of a material point are as follows (Eq. 4-5):

$$\boldsymbol{u} = \breve{\boldsymbol{x}}(\boldsymbol{x}_0, t) - \boldsymbol{x}_0 \equiv \boldsymbol{x} - \boldsymbol{x}_0 \tag{4}$$

$$\boldsymbol{v} = \frac{\partial \boldsymbol{u}}{\partial t} = \frac{\partial \boldsymbol{x}}{\partial t} \tag{5}$$

The plasticity models are usually written in a rate form for implementation of the finite elements code rather than to deal with increments of stress and strains. The spatial derivative of the velocity vector is a velocity gradient tensor ($\boldsymbol{L}$) (Eq. 6) [13]:

$$\boldsymbol{L} = \frac{\partial \boldsymbol{v}}{\partial \boldsymbol{x}} \equiv \nabla \boldsymbol{v} \tag{6}$$

where: ∇ is the spatial gradient operator and $\nabla = \frac{\partial}{\partial \boldsymbol{x}}$.

The $\boldsymbol{L}$ tensor might be expressed using the deformation gradient and its material time derivative ($\dot{\boldsymbol{F}}$) in line with the following formula (Eq. 7):

$$\boldsymbol{L} = \dot{\boldsymbol{F}} \cdot \boldsymbol{F}^{-1} \tag{7}$$

The velocity gradient tensor might be decomposed into symmetric deformation tensor ($\boldsymbol{D}$) and skew-symmetric spin tensor ($\boldsymbol{W}$) (Eq. 8-10).

$$\boldsymbol{L} = \boldsymbol{D} + \boldsymbol{W} \tag{8}$$

$$\boldsymbol{D} = sym\left(\boldsymbol{L}\right) = \frac{1}{2}\left(\boldsymbol{L} + \boldsymbol{L}^T\right) = \frac{1}{2}\left(\dot{\boldsymbol{F}} \cdot \boldsymbol{F}^{-1} + \boldsymbol{F}^{-T} \cdot \dot{\boldsymbol{F}}^T\right) \tag{9}$$

$$\boldsymbol{W} = skew\left(\boldsymbol{L}\right) = \frac{1}{2}\left(\boldsymbol{L} - \boldsymbol{L}^T\right) = \frac{1}{2}\left(\boldsymbol{F}^T \cdot \dot{\boldsymbol{F}} + \dot{\boldsymbol{F}}^T \cdot \boldsymbol{F}\right) \tag{10}$$

The gradient deformation tensor ($\boldsymbol{F}$) provides the complete information about the deformation including both the stretch and the rigid body rotation. The polar decomposition theory, which is one of the fundamental theorems of a large strain description, assumes that the $\boldsymbol{F}$ might be decomposed into an orthogonal rotation tensor ($\boldsymbol{R}$) and a symmetric stretch tensor (Eq. 11) [15].

$$\boldsymbol{F} = \boldsymbol{R}\boldsymbol{U} = \boldsymbol{V}\boldsymbol{R} \tag{11}$$

where: $\boldsymbol{U}$ and $\boldsymbol{V}$ are right and left symmetric, stretch tensors, respectively.

Based on the polar decomposition theorem, the right ($\boldsymbol{C}$) and left ($\boldsymbol{B}$) Cauchy-Green deformation tensors can be expressed as follows (Eq. 12-13).

$$\boldsymbol{F}\boldsymbol{F}^T = \boldsymbol{V}^2 = \boldsymbol{B} \tag{12}$$

$$\boldsymbol{F}^T\boldsymbol{F} = \boldsymbol{U}^2 = \boldsymbol{C} \tag{13}$$

The deformation gradient can be decomposed into elastic ($\boldsymbol{F}_e$) and plastic ($\boldsymbol{F}_p$) parts (Eq. 14):

$$\boldsymbol{F} = \boldsymbol{F}_e\boldsymbol{F}_p \,;\, det(\boldsymbol{F}_p) = 1 \text{ and } det(\boldsymbol{F}_e) > 0 \tag{14}$$

The rigid body rotation is contained in the plastic deformation gradient and therefore, the elastic deformation gradient includes only stretch (Eq. 15).

$$\boldsymbol{F}^e = \boldsymbol{V}^e \text{ and } \boldsymbol{F}^p = \boldsymbol{V}^p\boldsymbol{R} \tag{15}$$

Similarly, the $\boldsymbol{L}$ velocity gradient tensor is decomposed into elastic ($\boldsymbol{L}_e$) and plastic parts ($\boldsymbol{L}_p$) (Eq. 16), that can be additively decomposed to symmetric and skew-symmetric parts (Eq. 17-18):

$$\boldsymbol{L} = \boldsymbol{L}_e + \boldsymbol{F}_e\boldsymbol{L}_p\boldsymbol{F}_e^{-1} \,;\, \boldsymbol{L}_e = \dot{\boldsymbol{F}}_e\boldsymbol{F}_e^{-1} \text{ and } \boldsymbol{L}_p = \dot{\boldsymbol{F}}_p\boldsymbol{F}_p^{-1} \tag{16}$$

$$\boldsymbol{L}_e = \boldsymbol{D}_e + \boldsymbol{W}_e \,;\, \boldsymbol{D}_e = sym(\boldsymbol{L}_e) \text{ and } \boldsymbol{W}_e = skew(\boldsymbol{L}_e) \tag{17}$$

$$\boldsymbol{L}_p = \boldsymbol{D}_p + \boldsymbol{W}_p \,;\, \boldsymbol{D}_p = sym(\boldsymbol{L}_p) \text{ and } \boldsymbol{W}_p = skew(\boldsymbol{L}_p) \tag{18}$$

where: $\boldsymbol{D}_e$ and $\boldsymbol{D}_p$ are rates of elastic and plastic deformation gradient tensors; $\boldsymbol{W}_e$ and $\boldsymbol{W}_p$ are elastic and plastic spin tensors, respectively. For metallic materials in which $\varepsilon_p \gg \varepsilon_e$ and $\boldsymbol{F}_e \approx \boldsymbol{V}_e \approx \boldsymbol{U}_e \approx \boldsymbol{I}$ (Eq. 19-21) [13, 17]:

$$\boldsymbol{L} = \boldsymbol{L}_e + \boldsymbol{L}_p \tag{19}$$

$$\boldsymbol{D} = \boldsymbol{D}_e + \boldsymbol{D}_p \tag{20}$$

$$\boldsymbol{W} = \boldsymbol{W}_e + \boldsymbol{W}_p \tag{21}$$

The strain rate measure is the power conjugate of a Cauchy stress tensor and therefore, it is a rate of the deformation gradient tensor (Eq. 22-23) [13].

$$\dot{\boldsymbol{\varepsilon}} = \boldsymbol{D} \tag{22}$$

$$\dot{\boldsymbol{\varepsilon}} = \dot{\boldsymbol{\varepsilon}}_e + \dot{\boldsymbol{\varepsilon}}_p \rightarrow \dot{\boldsymbol{\varepsilon}}_e = \boldsymbol{D}_e \text{ and } \dot{\boldsymbol{\varepsilon}}_p = \boldsymbol{D}_p \tag{23}$$

where: $\dot{\boldsymbol{\varepsilon}}$, $\dot{\boldsymbol{\varepsilon}}_e$ and $\dot{\boldsymbol{\varepsilon}}_p$ are total, elastic and plastic strain rates, respectively.

2.2. Corotational formulation

The constitutive equations of large-strain plasticity are formulated in a rotation-neutralized configuration where the coordinate system located at each point of a continuum body is rotated with the material. The rotation of a material point is described by the orthogonal rotation tensor $\boldsymbol{R}$ which is subjected to the following evolutionary equation (Eq. 24):

$$\dot{\boldsymbol{R}} = \boldsymbol{\Omega}\boldsymbol{R} \tag{24}$$

where: $\boldsymbol{\Omega}$ is a spatial skew-symmetric second-order tensor associated with the orthogonal rotation tensor $\boldsymbol{R}$ as follows (Eq. 25):

$$\boldsymbol{\Omega} = \dot{\boldsymbol{R}}\boldsymbol{R}^T \,;\, \boldsymbol{R}^{-1} = \boldsymbol{R}^T \text{ and } \boldsymbol{\Omega} = -\boldsymbol{\Omega}^T \tag{25}$$

The Cauchy stress tensor ($\boldsymbol{\sigma}$) is rotated as follows (Eq. 26) [18]:

$$\underline{\boldsymbol{\sigma}} = \boldsymbol{R}^T\boldsymbol{\sigma}\boldsymbol{R} \tag{26}$$

where: $\underline{\boldsymbol{\sigma}}$ is a corotational representation of a Cauchy stress tensor.

The material rotation should be described by objective rates of the stress tensor. The Jaumann $\begin{pmatrix}\nabla J \\ \boldsymbol{\sigma}\end{pmatrix}$ and Green-Naghdi $\begin{pmatrix}\nabla G \\ \boldsymbol{\sigma}\end{pmatrix}$ rates of the Cauchy stress are defined as follows (Eq. 27-28):

$$\overset{\nabla J}{\boldsymbol{\sigma}} = \dot{\boldsymbol{\sigma}} + \boldsymbol{\sigma}\boldsymbol{W} - \boldsymbol{W}\boldsymbol{\sigma} \tag{27}$$

$$\overset{\nabla G}{\boldsymbol{\sigma}} = \dot{\boldsymbol{\sigma}} + \boldsymbol{\sigma}\boldsymbol{\Omega} - \boldsymbol{\Omega}\boldsymbol{\sigma} \tag{28}$$

where: $\dot{\boldsymbol{\sigma}}$ is time derivative of a Cauchy stress tensor and the other terms are corrections resulting from the finite rotations.

Materials models implemented in ABAQUS commercial software use Jaumann stress rate, while materials models written in the form of the user procedures employ Green-Naghdi stress rate. Thus, the results obtained by Jaumann and Green-Naghdi stress rates may differ, especially for large shearing deformations associated by large rotations. Unlike as in the Green-Naghdi stress rate an application of the Jaumann objective stress rate causes stress oscillations for large shear deformations in both elastic and plastic regimes. Thus, the material user procedure, which involves Green-Naghdi stress rate, takes the advantage over material commercial implementation in solving the problems with large shear deformations (in KOBO extrusion process large shears appear in processed material next to the rotating die).

2.3. Corotational representation of constitutive equations for the plasticity theory

Including the relationships: $\boldsymbol{R}^{-1} = \boldsymbol{R}^T$, $\boldsymbol{\sigma} = \boldsymbol{\sigma}^T$ and $\underline{\boldsymbol{C}} = \boldsymbol{C}$, the constitutive equations of the classical plasticity in the corotational form can be written as follows (the underscore means writing in a corotational form):

– The additive decomposition of the total strain ($\underline{\dot{\boldsymbol{\varepsilon}}}$) into elastic ($\underline{\dot{\boldsymbol{\varepsilon}}}_e$) and plastic parts ($\underline{\dot{\boldsymbol{\varepsilon}}}_p$) (Eq. 29):

$$\underline{\dot{\boldsymbol{\varepsilon}}} = \underline{\dot{\boldsymbol{\varepsilon}}}_e + \underline{\dot{\boldsymbol{\varepsilon}}}_p \tag{29}$$

– The Hooke's law (Eq. 30):

$$\underline{\dot{\boldsymbol{\sigma}}} = \boldsymbol{C} : \underline{\dot{\boldsymbol{\varepsilon}}}_e \tag{30}$$

where: $\boldsymbol{C}$ is the constitutive matrix.

– The yield condition assuming the kinematic and isotropic hardening (Eq. 31):

$$\Phi = J_2\left(\overline{\boldsymbol{\sigma}} - \boldsymbol{x}\right) - \sigma_y - r, \quad \text{where: } \Phi \begin{cases} < 0 - \textit{elastic response} \\ = 0 - \textit{plastic response} \end{cases} \tag{31}$$

where: $\boldsymbol{x}$ is a backstress and r is isotropic hardening.

– The effective plastic strain (Eq. 32):

$$\dot{\bar{\varepsilon}}_p = \sqrt{\frac{2}{3}} \left\| \underline{\dot{\boldsymbol{\varepsilon}}_{\boldsymbol{p}}} \right\| \tag{32}$$

where: $\dot{\bar{\varepsilon}}_p$ is the effective plastic strain and $\underline{\dot{\varepsilon}_p}$ is the rate of plastic strain in a corotational form.

– The consistency condition assuming both isotopic and kinematic hardening (Eq. 33):

$$\frac{\partial \Phi}{\partial \underline{\boldsymbol{\sigma}}} : \partial \underline{\boldsymbol{\sigma}} + \frac{\partial \Phi}{\partial \underline{\boldsymbol{x}}} : \partial \underline{\boldsymbol{x}} + \frac{\partial \Phi}{\partial \dot{\bar{\varepsilon}}_p} : \partial \dot{\bar{\varepsilon}}_p = 0 \tag{33}$$

– The normal vector $\underline{\boldsymbol{N}}$(Eq. 34):

$$\underline{\boldsymbol{N}} = \frac{3}{2} \frac{\underline{\overline{\boldsymbol{\sigma}}^{\boldsymbol{d}}} - \underline{\boldsymbol{x}}}{\overline{\boldsymbol{\sigma}}} \tag{34}$$

– The plastic strain increment $\underline{\dot{\boldsymbol{\varepsilon}}_{\boldsymbol{p}}}$ (Eq. 35):

$$\underline{\dot{\boldsymbol{\varepsilon}}_{\boldsymbol{p}}} = \frac{3}{2} \frac{\dot{\overline{\boldsymbol{\varepsilon}}_{\boldsymbol{p}}}}{\overline{\boldsymbol{\sigma}}} \boldsymbol{\sigma}^d \tag{35}$$

where: $\boldsymbol{\sigma}^d$ is a deviatoric stress.

– The stress increment $\underline{\dot{\boldsymbol{\sigma}}}$ (Eq. 36):

$$\underline{\dot{\boldsymbol{\sigma}}} = 2G\underline{\dot{\boldsymbol{\varepsilon}}_{\boldsymbol{e}}^{\boldsymbol{d}}} + \left(K - \frac{2}{3}G\right)\dot{\varepsilon}^v \boldsymbol{I} \tag{36}$$

where: G and K are bulk and shear modulus, respectively.

– The evolution of the backstress for the Chaboche model is described as follows (Eq. 37):

$$\underline{\dot{\boldsymbol{x}}_{\boldsymbol{i}}} = \frac{2}{3}\underline{\dot{\boldsymbol{\varepsilon}}_{\boldsymbol{p}}} - c_i \gamma_i \dot{\bar{\varepsilon}}_p, \quad \underline{\dot{\boldsymbol{x}}} = \sum_{i=1}^{n} \underline{\dot{\boldsymbol{x}}_{\boldsymbol{i}}} \tag{37}$$

where: c_i and γ_i are material constants.

The previous authors' tests [13,22] showed that two hardening rules were sufficient in simulations of hysteresis curves in symmetrical cyclic loading/unloading tests. The introduction of the third backstress is recommended in numerical calculations of asymmetrical cyclic phenomena, e.g. the ratcheting and the stress relaxation. The Chaboche model with two backstresses x_1 and x_2 is used in numerical simulations presented in this paper.

– The evolution of isotropic hardening $\dot{r}\left(\dot{\bar{\varepsilon}}_p\right)$ is determined by the Voce isotropic law (Eq. 38):

$$\dot{r}\left(\dot{\bar{\varepsilon}}_p\right) = b\left(Q - r\right)\dot{\bar{\varepsilon}}_p \tag{38}$$

where: Q is a saturated value of the isotropic hardening component and b determines the rate where the saturation is achieved.

– During the plastic deformation of a material, the heat is released. The heat generation caused is calculated as follows (Eq. 39):

$$q = \eta(\boldsymbol{\sigma} - \boldsymbol{x}) : \dot{\boldsymbol{\varepsilon}}^p \tag{39}$$

where: q is a heat volume rate, $\boldsymbol{\sigma}$ is the Cauchy stress, $\boldsymbol{x}$ is a backstress associated with the kinematic hardening and η is a Taylor-Quinney coefficient (usually $\eta = 0.9$).

2.4. The Coupled Eulerian-Lagrangian method

The Lagrangian and Eulerian formulations are mainly used in FEM problems of the continuum mechanics. In the Lagrangian approach, the equations are written in terms of the referential configuration and the material point moves in a space in time. The equations in the Eulerian description are defined in terms of the current position.

The main difference between Lagrangian and Eulerian formulations concerns the elements mesh. The Lagrangian mesh deforms with the material during the deformation while the Eulerian mesh is fixed in a space and the material flows through it. The Eulerian meshes can be used in large deformation analyses without remeshing while the Lagrangian ones cannot due to their large distortions.

For the FEM analysis of the KOBO extrusion process, the Coupled Eulerian-Lagrangian (CEL) approach is used here. The method includes advantages of both Lagrangian and Eulerian formulations. The main equations associated with the CEL method are the following [19]:

– The relation between material (Lagrangian) and spatial (Eulerian) time derivatives (Eq. 40):

$$\frac{D\boldsymbol{\Phi}}{Dt} = \frac{\partial \boldsymbol{\Phi}}{\partial t} + \mathbf{v} \cdot \left(\nabla \boldsymbol{\Phi}\right) \tag{40}$$

where: $\boldsymbol{\Phi}$ is the arbitrary solution variable, $\mathbf{v}$ is the material velocity, $\frac{D\boldsymbol{\Phi}}{Dt}$ and $\frac{\partial \boldsymbol{\Phi}}{\partial t}$ are material and spatial derivatives.

– The Lagrangian mass, momentum and energy conservation laws in the Eulerian spatial formulation (Eq. 41-43):

$$\frac{\partial \rho}{\partial t} + \boldsymbol{v} \cdot \left(\nabla \rho\right) + \rho \nabla \cdot \boldsymbol{v} = 0 \tag{41}$$

$$\frac{\partial \boldsymbol{v}}{\partial t} + \boldsymbol{v} \cdot \left(\nabla \cdot \boldsymbol{v}\right) = \frac{1}{\rho}\left(\nabla \cdot \boldsymbol{\sigma}\right) + \boldsymbol{b} \tag{42}$$

$$\frac{\partial e}{\partial t} + \boldsymbol{v} \cdot \left(\nabla e\right) = \boldsymbol{\sigma} : \boldsymbol{D} \tag{43}$$

where: ρ is density, $\boldsymbol{\sigma}$ is the Cauchy stress, $\boldsymbol{b}$ is the vector of body forces, e is the strain energy and $\boldsymbol{D}$ is a velocity strain.

– The Eulerian mass, momentum and energy conservation laws (Eq. 44-46):

$$\frac{\partial \rho}{\partial t} + \nabla \cdot \left(\rho \boldsymbol{v}\right) = 0 \tag{44}$$

$$\frac{\partial \rho \boldsymbol{v}}{\partial t} + \nabla \cdot \left(\rho \boldsymbol{v} \otimes \boldsymbol{v} \right) = \nabla \cdot \boldsymbol{\sigma} + \rho \boldsymbol{b} \tag{45}$$

$$\frac{\partial e}{\partial t} + \nabla \cdot \left(e \boldsymbol{v} \right) = \boldsymbol{\sigma} : \boldsymbol{D} \tag{46}$$

The general form of Eq. 44-46 (Eq. 47):

$$\frac{\partial \varphi}{\partial t} + \nabla \cdot \boldsymbol{\Phi} = \boldsymbol{S} \tag{47}$$

where: $\boldsymbol{\Phi}$ is the flux function and $\boldsymbol{S}$ is the source term.

– The division of Eq. 47 into two separate problems is made using the splitting operator (Eq. 48-49):

$$\frac{\partial \varphi}{\partial t} = \boldsymbol{S} \tag{48}$$

$$\frac{\partial \varphi}{\partial t} + \nabla \cdot \boldsymbol{\Phi} = 0 \tag{49}$$

The Eq. (48) contains the source term represents the Lagrangian step and the Eq. (49) contains the convective one which represents the Eulerian step [20]. It is worth noting that Eq. (47) is not the superposition of Eq. (48) and Eq. (49). In the CEL approach Eq. (47) is solved in two steps which represent two separated problems: Lagrangian (Eq. 48) following the Eulerian (Eq. 49) one. The Lagrangian mesh which deforms in time, is used to fill the Eulerian mesh with the processed material. It is also important that the Lagrangian mesh, which is not available for the ABAQUS user, deforms under the load and from time to time after becoming too distorted, requires remeshing.

The main advantages of the CEL formulation used in numerical simulations of the KOBO extrusion are a very good convergence and the stability of the solution. On the other hand, the CEL approach used in Abaqus program, is based on the conditionally stable dynamic explicit method and therefore takes very small stable time increments [13]. It extents the time of computations. In the dynamic explicit approach, the nodal displacements for the time $t + \Delta t$ are calculated for displacements known from the last two integration steps (time t and $t - \Delta t$). The damping is neglected and the lumped mass matrix (diagonal form) is used. It causes that equations which update nodal displacement for the time $t + \Delta t$ are independent. In the dynamic explicit procedure there is even no need to form the global stiffness matrix and its factorization which for a large problems requires a lot of computations and introduces round-off errors.

3. Results and discussion

In order to perform the numerical calculations of the KOBO extrusion process, the first step of this research was an identification of hardening parameters for Chaboche and Voce models. They can be determined on the basis of experimental research e.g. cyclic tension-compression tests carried out for various temperature. Here, we use the results available in literature for an alternative elastic-plastic material model – namely Bodner-Partom (B-P) material model. The numerically generated curves for the B-P model parameters contained in [21] are applied in this study with the aim of obtaining pseudo-experimental hysteresis curves for a AMG-6 alloy at different temperatures (Fig. 2). They were then used as pseudo-experimental curves for initial selection of hardening parameters with the use of the ABAQUS program (TABLE 1). The good convergence between pseudo-experimental and numerical hysteresis curves was achieved.

TABLE 1

Hardening Parameters for different temperatures

Hardening parameters	Temperature [°C]		
	20	300	400
c_1 [MPa]	34382.0	166.4	47.3
γ_1 [-]	980.3	18.6	0
c_2 [MPa]	37195.0	28016.0	13013.0
λ_2 [-]	2970.3	849.7	401.8
Q [MPa]	180.0	140.0	65.0
b [-]	39.0	48.0	90.0

In order to enhance hardening parameters, the proprietary original methodology was developed. The detailed information about the procedure is contained in [22]. The optimization formulation using the least-square method was applied to get a better agreement of the pseudo-experimental and numerical curves. The error norm between pseudo-experimental and approximated stress values is defined using Eq. (50):

$$\|B\| = \sqrt{\int_{\varepsilon} \left(\sigma_{exp} - \sigma_{app} \right)^2 d\varepsilon} \tag{50}$$

where: σ_{exp} and σ_{app} are pseudo-experimental and approximated stress values.

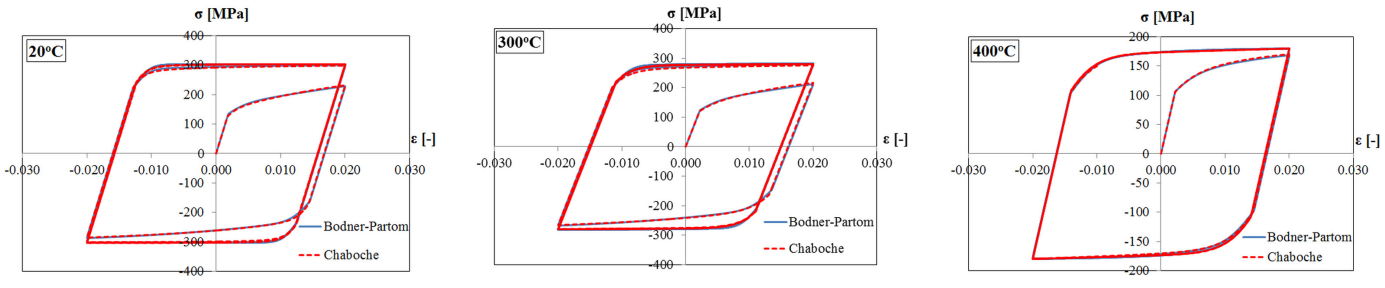

(a) (b) (c)

Fig. 2. Pseudo-experimental and numerical hysteresis stress-strain curves for different temperatures; 20°C (a), 300°C (b) and 400°C (c). Experimental data based on [21]

TABLE 2

Hardening Parameters for different temperatures determined using the optimization approach

Hardening parameters	20°C				
	Set 1	**Set 2**	**Set 3**	**Set 4**	**Set 5**
c_1 [MPa]	21230.4	20602.2	20935.4	29937.2	29570.4
γ_1 [-]	654.8	1077.6	778.0	901.1	1137.6
$c2$ [MPa]	22889.2	24989.7	37408.6	23186.3	26447.0
γ_2 [-]	2617.8	1410.5	3442.3	3140.0	2625.8
Q [MPa]	142.4	139.9	144.9	141.2	137.4
b [-]	32.2	42,4	33.6	34.6	45.1
	300°C				
c_1 [MPa]	94.0	59.8	152.4	122.3	177.9
γ_1 [-]	11.4	17.5	14.6	18.3	17.9
c_2 [MPa]	24253.4	14207.8	19035.4	17236.3	12034.3
γ_2 [-]	797.4	583.4	606.3	645.3	601.2
Q [MPa]	128.9	133.1	126.5	130.7	135.9
b [-]	39.6	44.7	44.0	42.2	44.3
	400°C				
c_1 [MPa]	51.5	39.4	35.8	53.1	33.2
γ_1 [-]	0	0	0	0	0
c_2 [MPa]	7943.6	11344.2	13031.03	9384.7	10879.6
γ_2 [-]	269.5	321.2	364.3	300.5	334.9
Q [MPa]	43.5	35.8	33.2	40.8	38.2
b [-]	75.2	93.5	69.9	82.1	84.9

The optimization procedure improved the convergence of hysteresis curves, but a similar small error norm can be obtained for different sets of hardening parameters (see TABLE 2). Thus, the important question arises: which set of the hardening parameters gives the best approximation? For the selection of this optimal set, the authors' method based on the fuzzy logic was applied. This approach assumes some uncertainty of the hardening data. The hardening parameters for Chaboche and Voce models are assumed to be fuzzy input. After the fuzzy analysis is performed, the fuzzy output variable (the error norm B), as well as its membership function are obtained. The discrete (crisp) value (B) of the error norms is found in the defuzzification step with by means of the mass center method (Eq. 51):

$$B = \frac{\int B \cdot \mu(B)\, dz}{\int \mu(B)\, dz} \tag{51}$$

where $\mu(B)$ is the membership function of B variable. The set of hardening parameters for which the crisp value of the fuzzy error is the smallest, is assumed as the most reliable solution (TABLE 3). Hardening parameters of Chaboche model calibrated this way were then used in numerical simulations of the KOBO extrusion as material data.

For solving dynamic problems, a user material model written using the FORTRAN language was applied as a VUMAT procedure. It comprises constitutive equations contained in Section 2 and works both for small and large displacements. In the VUMAT procedure for given strain increments, the plastic strain increments should be determined and after that, the stress increments in the corotational frame should be computed. The

TABLE 3

Hardening Parameters determined using the fuzzy logic method

Hardening parameters	Temperature [°C]		
	20	**300**	**400**
c_1 [MPa]	28695.3	121.1	34.5
γ_1 [-]	999.7	20.0	0
c_2 [MPa]	31935.9	22862.4	8783.6
γ_2 [-]	2464.5	561.6	271.2
Q [MPa]	154.0	114.6	37.5
b [-]	40.3	50.8	76.3

stress transformation to the global coordinate system is automatically made by Abaqus (Eq. 28). All internal state variables must be updated at the end of the integrations step (yield stress, back stress components, effective plastic strain).

The following integration schemes were derived and implemented in the user routine: explicit, implicit and semi-implicit. The explicit procedure which is conditionally stable uses derivatives taken from the beginning of the integration step. The unconditionally stable and more accurate implicit integration which consists of two steps: elastic predictor and plastic corrector uses derivatives computed at the end of the integration step. The third type of integration which is called semi-implicit, is based on the assumption that for a very small time (load) increment both isotropic and kinematic hardenings are locally linear. It allows for an analytical derivation of the plastic multiplier (with the assumption that normal to the yield surface does not change during the integration step). This approach is less computationally expensive than others. All integration approaches of constitutive equations provide similar results due to the very small time increment used by ABAQUS program – 10^{-6} (few orders below the stable time increment required by explicit integration of the constitutive equations).

The correctness of procedure written was tested on several boundary value problems. As an example in Fig. 3 a plate with holes restrained at one end and subjected to a tension is presented. Similar results are obtained for both Chaboche user material procedure and for Chaboche material model available in a ABAQUS program. The comparison of H-M-H stress and the effective plastic strain for a user material and the ABAQUS one is shown in Fig. 3 and 4. In both cases, an excellent convergence between Abaqus material model and user-defined material one has been obtained. A noticeable difference in effective plastic strain plots is that the minimum plastic strain for the user material is slightly below zero. It is caused by the extrapolation of the results from the Gaussian points to nodes (negative equivalent plastic strains in Gaussian points have been never computed).

The numerical simulation of the KOBO extrusion were done using the 3-dimensional model (Fig. 5a) in which tools; a recipient, a die and a punch, were modelled as rigid bodies. The Eulerian part covers the initial position of the material and its location after the extrusion. The 8-node Eulerian hexahedral elements considering thermomechanical coupling were used in Eulerian domain. Different meshes were tested in numerical

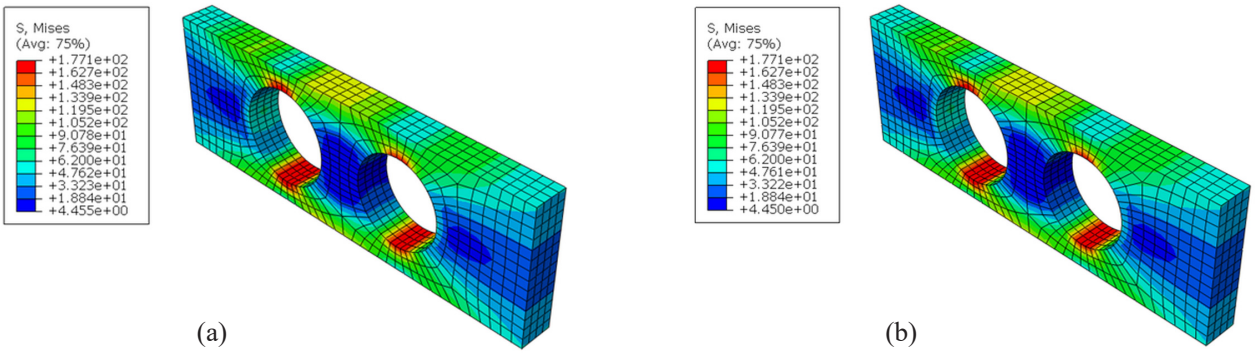

Fig. 3. Comparison of the H-M-H stress obtained for a user material (a) and for material available in ABAQUS (b)

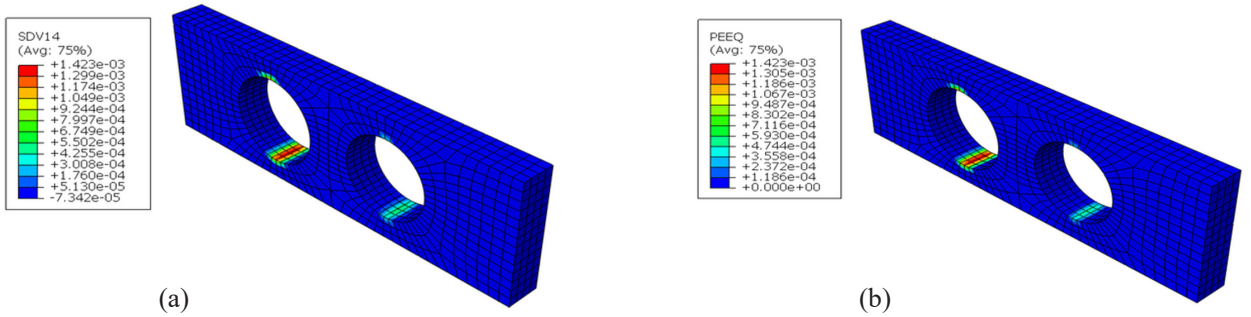

Fig. 4. Comparison of the effective plastic strain obtained for a user material (a) and for material available in ABAQUS (b)

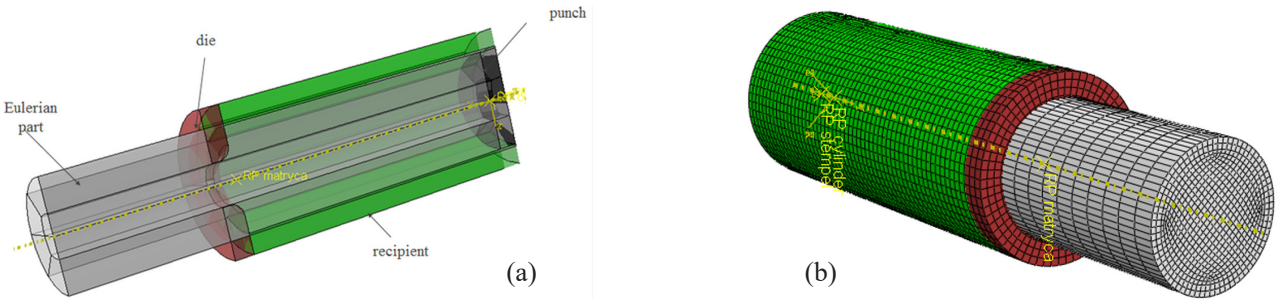

Fig. 5. Numerical model (a) and mesh (b) applied in this work

simulations but finally calculations were done for cylindrical mesh thickening to the core (Fig. 5b). Some data concerning numerical model are contained in TABLE 4.

Exemplary results presented in this section are obtained by the application of Chaboche material model implemented commercially in Abaqus program. However, very similar results are reached with use of the user material procedure. The H-M-H stress distribution in the KOBO extrusion is shown in Fig. 6a. The highest stress values occur near the die hole and decrease towards the center of the recipient. Fig. 6b shows the distribution of equivalent plastic strain. The plastic strain occurs mostly in the narrow area of the extruded material.

The temperature distribution in the extruded material is shown in Fig. 7. As it is not possible in the CEL procedure to take into account the heat flow from the material to tools, the temperature values might be overestimated here.

The advantage of the user material procedure over material model, which is commercially implemented in a FEM program,

TABLE 4

Details of the numerical model applied in this research

Feature	Description
Type of model	3D
Material model	Chaboche elastic-plastic
Integration procedure	Dynamic explicit
Friction model	Coulomb model
Type of tools	Rigid bodies
Number of calculation steps	2 steps
Time of calculation step	0.5 s
Stable time increment	$1.9 \cdot 10^{-9}$ s
Total time of calculations	10 hours
Other material data	E = 61 700 MPa, ν = 0.3, ρ = 2,700 kg/m^3
Thermal data	c_p = 909 J/(kg·K), h = 206 W/(m·K), $\alpha = 4.5 \cdot 10^{-6}$
* E – Young modulus, ν – Poisson's ratio, ρ – density, c_p – specific heat, h –thermal conductivity coefficient, α – linear expansion coefficient	

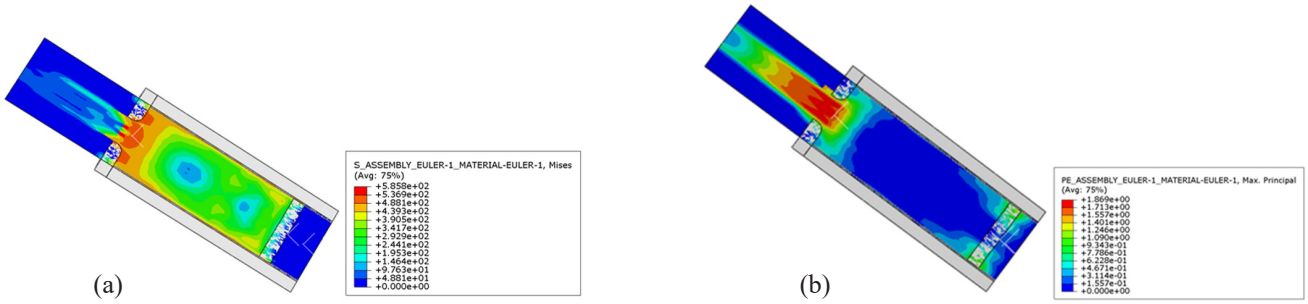

(a) (b)

Fig. 6. The von Mises (a) and the equivalent plastic strain (b) distribution in the KOBO process

is the possibility to obtain more information about the material behaviour during the KOBO extrusion. In the wake of the die movement, extruded material stabilizes very quickly near the die hole due to its isotropic hardening (Fig. 8) which reaches its saturation. Such information cannot be obtained in commercial implementation of the Chaboche model. Large isotropic hardening up to the saturation increases the yield stress and worsens the conditions for continuing the KOBO process by increasing the forces acting on the tools.

The shape of plastic zones obtained in numerical simulations was confirmed in the experimental research (Fig. 9). The plastic strain zones have characteristic rounded shape visible both in numerical and experimental results. According to [23], the characteristic shape of plastic flow streams is associated with the dominant crystal orientation which follows with the stream of the material.

4. Summary and conclusions

Numerical simulations of the KOBO extrusion process for AMG-6 aluminum alloy using the thermomechanical coupled Lagrangian-Eulerian (CEL) formulation is presented here. The calculations were done with the use of the Chaboche elastic-plastic material model with two backstresses in with material parameters determined for various temperature. The numerical simulations were done using the user material procedure whose correctness was verified in selected elastic-plastic problems. The following integration procedures of the constitutive equations were investigated: explicit, implicit and semi-implicit (local linearization). The heat was generated due to plastic work and the friction between processed material and tools.

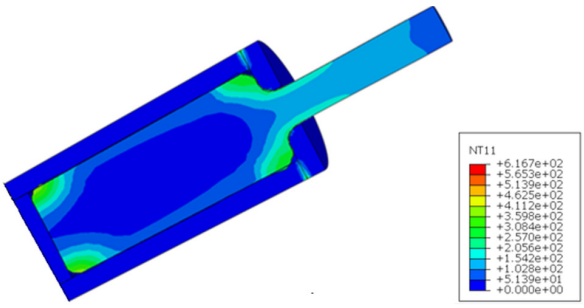

Fig. 7. The temperature distribution in the KOBO extrusion

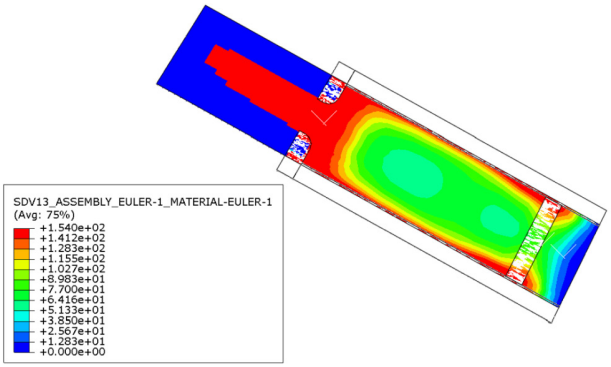

Fig. 8. The isotropic hardening in the extruded material

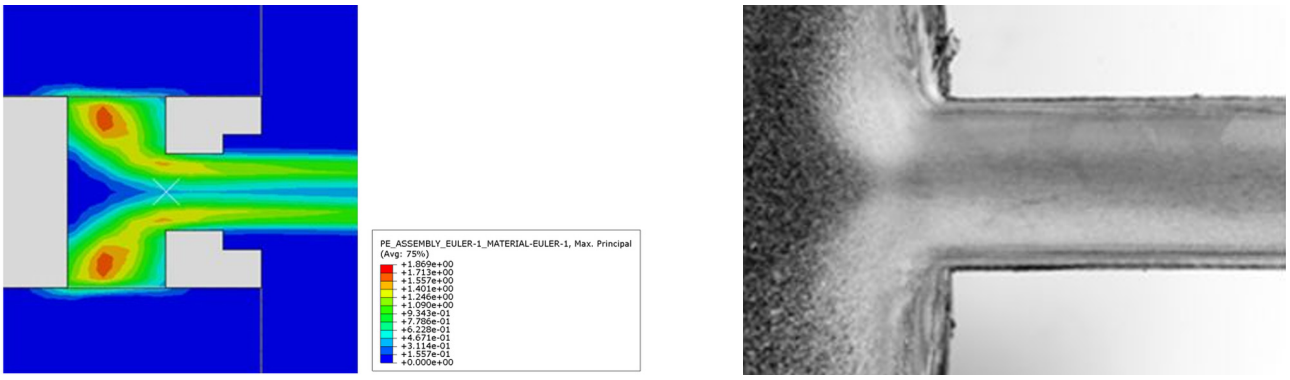

(a) (b)

Fig. 9. The shape of plastic zones; numerical (a) and experimental (b) results [23]

On the basis of the results obtained, the following conclusions can be drawn:

1) The CEL formulation enables to model the KOBO extrusion process and provides reliable results in stresses and strains. The results of temperature are slightly overestimated because the CEL approach does not allow modelling the heat flow from the processed material to the tools.
2) The knowledge about the hardening parameters of the material might have a key influence on the selection of the conditions of the KOBO process – materials with dominant isotropic hardening are hard to extrude.
3) The modelling of the KOBO process using the user material procedure allow better knowledge about the extruded material response.

The results obtained in numerical simulations using the material user procedure can help to optimize the conditions of the KOBO extrusion and can lead to the elimination of possible problems associated with the life of tools.

REFERENCES

[1] K. Pieła, L. Błaż, M. Jaskowski, Arch. Metall. Mater. **58** (3), 683-689 (2-13).

[2] W. Bochniak, A. Brzostowicz, Arch. Metall. Mater. **55** (2), 587-600 (2010).

[3] W. Bochniak, A. Korbel, P. Ostachowski, S. Ziółkiewicz, Obrób. Plast. Met. **24** (2), 83-87 (2013).

[4] M. Zwolak, R.E. Śliwa, Obrób. Plast. Met. **28** (4), 371-330 (2017).

[5] P. Długosz, W. Bochniak, P. Ostachowski, R. Molak, M.D. Guigou, M. Hebda, Materials **14** (21), 6543 (2021).

[6] A. Šupić, A. Bečirović, A. Obućina, M. Zrilić, Procedia Struct. Integr. **13**, 2077-2082 (2018).

[7] P.F. Zheng, L.C. Chan, T.C. Lee, Finite Elem Anal Des **42** (3), 189-207 (2005).

[8] G. Ryzińska, A. Skrzat, R.E. Śliwa, Obrób. Plast. Met. **26** (1), 73-92 (2015).

[9] A. Skrzat, RUT Mechanika **84** (4), 25-35 (2012).

[10] K. Kowalczyk-Gajewska, S. Stupkiewicz, Arch. Metall. Mater. **58** (1), 113-118 (2013).

[11] H. Petryk, S. Stupkiewicz, Int. J. Mat. Res. **103** (3), 271-277 (2012).

[12] J. Maciejewski, Z. Mróz, J. Mater. Process. Technol. **206** (1-3), 333-344 (2008).

[13] M. Wójcik, A. Skrzat, ASTRJ **15** (1), 197-208 (2021).

[14] S.A.H. Montaman, K. Schacht, C. Haase, U. Prahl, Int J Solids Struct **178/179**, 59-80 (2019).

[15] F. Dunne, N. Petrinic, Introduction to Computational Plasticity, Oxford University Press (2005).

[16] T. Belytschko, W.K. Liu, B. Moran, K.I. Elkhodary, Nonlinear Finite Elements for Continua and Structures. Second Edition, Wiley (2014).

[17] E.A. de Souza Neto, D. Perić, D.R.J. Owen, Computational Methods for Plasticity. Theory and Applications, Wiley (2008).

[18] J.C. Simo, T.J.R. Hughes, Computational Inelasticity, Springer (1998).

[19] D.J. Benson, Comput Methods Appl Mech Eng **140** (1-2), 59-86 (1997).

[20] A. Skrzat, RUTMech **84** (4), 25-35 (2012).

[21] S.R. Bodner, Unified Plasticity for Engineering Applications, Springer (2002).

[22] M. Wójcik, A. Skrzat, Acta Mech. **232** (2), 685-708 (2021).

[23] A. Korbel, J. Pospiech, W. Bochniak, A. Tarasek, P. Ostachowski, J. Bonarski, Int. J. Mat. Res. **102**, 464-473 (2011).